



Photocatalytic CO_2 reduction promoted by uniform perovskite hydroxide $\text{CoSn}(\text{OH})_6$ nanocubes



Xiahui Lin^{a,b}, Yilin Gao^a, Min Jiang^a, Yongfan Zhang^a, Yidong Hou^a, Wenxin Dai^a, Sibo Wang^a, Zhengxin Ding^{a,*}

^a State Key Laboratory of Photocatalysis on Energy and Environment, College of Chemistry, Fuzhou University, Fuzhou 350002, PR China

^b College of Chemistry & Materials Science, Longyan University, Longyan 364012, PR China

ARTICLE INFO

Keywords:
Perovskite
 $\text{CoSn}(\text{OH})_6$
 CO_2 reduction
Photocatalysis
Nanocubes

ABSTRACT

Herein, we report the facile synthesis of uniform perovskite hydroxide $\text{CoSn}(\text{OH})_6$ nanocubes and their first use as noble-metal-free, highly efficient and stable catalysts for the deoxygenative reduction of CO_2 to CO with visible light. The $\text{CoSn}(\text{OH})_6$ sample is synthesized through a one-pot co-precipitation method and fully characterized by various techniques including XRD, FTIR, FESEM, TEM, EDX, EDX-mappings, XPS, DRS, and N_2 sorption measurements. The $\text{CoSn}(\text{OH})_6$ solid is found by theoretical calculations to be capable of absorbing and activating CO_2 molecules on the (100) surface. Under the optimal reaction conditions, the $\text{CoSn}(\text{OH})_6$ catalyst exhibits a high CO_2 reduction activity with visible light irradiation, affording a CO generation rate of $18.7 \mu\text{mol h}^{-1}$. The stability and reusability of the $\text{CoSn}(\text{OH})_6$ catalyst for photocatalytic CO_2 reduction are solidly confirmed. Results of *in situ* photoluminescence spectroscopy and photocurrent response characterizations indicate that the $\text{CoSn}(\text{OH})_6$ catalyst can efficiently promote the separation and transfers of photoexcited charge carriers during photocatalysis, and eventually leading to obviously enhanced CO_2 photoreduction performance. Moreover, a possible mechanism for the photocatalytic CO_2 reduction reaction is also proposed based on the results of activity evaluation and photo-/electro-chemical measurements.

1. Introduction

Photocatalytic reduction of CO_2 to generate valuable chemicals has always been considered as one of the most promising methods to exploit renewable alternatives to fossil fuels and alleviate global warming effect [1–4]. However, the achieved CO_2 reduction efficiency by artificial catalysts is still too low to practical applications, mainly due to the chemical inertness of linear CO_2 molecules as well as the high recombination rate of photo-induced charge carriers during photoredox processes [5–8]. Therefore, the efficient CO_2 photoreduction catalysis typically involves the harmonious combination of light harvesters, catalysts/cocatalysts, electron mediators and CO_2 activators in a tandem system, which can effectively prevent the formation of high-energy intermediates, and thus promoting the catalytic efficiency [9–20].

Transition metal ions/complexes have been actively investigated as functional cofactors to promote photochemical conversion of CO_2 co-operated with appropriate light harvesters, owing to their excellent electron mediating capabilities [21–26]. Recently, metal oxides and metal organic frameworks exhibit enormous vitality as efficient

heterogeneous catalytic materials to operate CO_2 transformation reactions with inspiring achievements, benefiting from the high photochemical activity and stability, easy separation and reusability, and CO_2 -activating capability [12,14,27–31]. Despite these advances, it is still highly desirable to develop new heterogeneous catalysts made of earth abundant elements to further improve the quantum efficiency of CO_2 photoreduction reactions.

As a unique class of functional materials, perovskite materials have aroused significant research interests in energy storage and conversion areas in recent years, because of their stable crystal structure, excellent electromagnetic properties, and high catalytic activities for target reactions [32–34]. However, the employment of a well-defined three-dimensional (3D) perovskite-type material as an efficient catalyst for use in photocatalytic CO_2 reduction application is still in its early stage, but is very promising. Herein, we demonstrate the facile synthesis of uniform perovskite hydroxide $\text{CoSn}(\text{OH})_6$ nanocubes and their first utilization as non-noble-metal, highly efficient and stable catalysts to promote photocatalytic reduction of CO_2 under mild conditions. The $\text{CoSn}(\text{OH})_6$ nanocube materials are synthesized by a one-pot co-precipitation method and fully characterized by various physicochemical

* Corresponding author.

E-mail addresses: zxding@fzu.edu.cn, zxding10@163.com (Z. Ding).

techniques (e.g., XRD, FTIR, SEM, TEM, EDX, EDX-mappings, XPS, DRS, and N_2 sorption measurements). Under the optimal reaction conditions, the CoSn(OH)_6 catalyst exhibits a high CO generation rate of $18.7 \mu\text{mol h}^{-1}$ by the cooperation with a visible light photosensitizer. The stability and reusability of the CoSn(OH)_6 perovskite material for the photocatalytic CO_2 -to-CO conversion catalysis are solidly confirmed. Results of *in situ* photoluminescence (PL) spectroscopy and photocurrent responses characterizations demonstrate that CoSn(OH)_6 catalyst can efficiently facilitate the separation and migration of excited charge carriers during photocatalysis, and eventually resulting in obviously enhanced CO_2 photoreduction performance. Moreover, a possible mechanism for the photocatalytic CO_2 reduction reaction is also proposed based on the results of activity evaluation and photo-/electrochemical measurements.

2. Experimental section

2.1. Materials, synthesis, and characterizations

All of the reagents are analytical grade and are used without further purification. Stannic chloride pentahydrate ($\text{SnCl}_4 \cdot 5\text{H}_2\text{O}$, 98%) were purchased from Aladdin. Cobalt chloride ($\text{CoCl}_2 \cdot 6\text{H}_2\text{O}$, 97%) and acetonitrile (MeCN) were provided by Alfa Aesar. The super grade purity carbon dioxide gas (99.999%) was supplied by Fuzhou Lianzhong Industrial Gases Co. Ltd. The $^{13}\text{CO}_2$ (98% enriched) was purchased from Hess chemical gas center in Beijing.

Perovskite hydroxide CoSn(OH)_6 nanocubes were synthesized through a one-pot co-precipitation method [35]. In a typical synthesis, 10 ml of ethanol solution of $\text{SnCl}_4 \cdot 5\text{H}_2\text{O}$ (2 mmol) was added into 70 ml of a mixture aqueous solution of CoCl_2 (2 mmol) and sodium citrate (2 mmol) under magnetically stirring for 15 min, followed by dropwise addition of 10 ml of aqueous solution of NaOH (2 M) with a certain creep rate at room temperature. After about 1 h, the resulting pink precipitate was harvested by centrifugation and washed with deionized (DI) water and ethanol several times and then dried in vacuum oven at 60°C overnight for further use.

A Bruker D8 Advance instrument ($\text{Cu K}\alpha_1$ irradiation, $\lambda = 1.5406 \text{ \AA}$) was used to collect the X-ray diffraction (XRD) patterns of samples. The accelerating voltage and the applied current were 40 KV and 40 mA, respectively. Data were recorded at a scanning rate of $0.02^\circ 2\theta \text{ s}^{-1}$ in the 2θ region of $15\text{--}80^\circ$. A Hitachi New Generation SU8010 field emission scanning electron microscope (SEM) was employed to capture the FEMSEM images and energy dispersive X-ray (EDX) spectrum. Transmission electron microscopy (TEM) measurements were conducted using a JEOL model JEM 2010 EX instrument at an accelerating voltage of 200 KV with the sample supported on a copper grid. X-ray photoelectron spectroscopy (XPS) characterizations were carried out on a PHI Quantum 2000 XPS system with a monochromatic Al $K\alpha$ source and a charge neutralizer. The X-ray photoelectron spectra of all of the elements were referenced to the C 1s peak arising from adventitious carbon (its binding energy was set at 284.6 eV). Specific surface area and pore size distribution curve of the samples were determined from the results of N_2 sorption measurements at 77 K (Micromeritics ASAP 2020) by using the Brunauer-Emmett-Teller (BET) and Barrett-Joyner-Halenda (BJH) methods. UV-vis diffuse reflectance spectra (DRS) spectra were obtained on a Varian Cary 500 UV-Vis-NIR spectrophotometer with BaSO_4 as a reflectance standard. The absorbance spectrum of the Ru-dye solution was recorded by a Varian Cary 50 UV-vis spectrophotometer. Mott-Schottky measurements were conducted on a Zennium electrochemical workstation (Zahner Co.). The measurements were performed in a conventional three electrodes cell using Pt plate and Ag/AgCl electrode as the counter electrode and reference electrode, respectively. For Mott-Schottky experiment, the potential ranged from -0.4 to 0.1 V (vs. Ag/AgCl), and the frequency were 0.5, 1.0, and 1.5 kHz, respectively. Prior to all measurements, the electrolyte (0.2 M Na_2SO_4 aqueous solution)

was purged with nitrogen gas for 30 min.

Gas chromatographic (GC) analysis was conducted using an Agilent 7820A gas chromatography equipped with a thermal conductivity detector (TCD) and a TD-01 packed column. High purity Ar was used as the carrier gas. The oven temperature was set constant at 50°C , and the inlet and detector temperature were set at 120°C and 200°C , respectively. A HP 5973 GC-MS was used to analyze the products of the $^{13}\text{CO}_2$ isotopic experiment.

2.2. Computational details

Periodic first-principles calculations based on density functional theory (DFT) were carried out using the projector-augmented wave (PAW) formalism. The generalized gradient approximation Perdew-Burke-Ernzerhof (PBE) type exchange-correlation was adopted. The kinetic cut-off energy for the plane-wave expansion was set to 400 eV, and a $(3 \times 3 \times 1)$ Monkhorst-Pack k-point grid was used. The effects of spin polarization were considered and the dipole correction in the surface normal direction was applied. To properly describe the electron correlation of partially occupied Co 3d states, the PBE plus on-site repulsion U (PBE + U) method was adopted. In here, the PBE + U calculations were carried out following the simplified rotationally invariant form proposed by Dudarev to address the self-interaction energy, and the effective single parameter U-J of 3.0 eV was used for Co atom. The convergence thresholds of the energy change and the maximum force for the geometry optimizations were set to 10^{-5} eV and $0.05 \text{ eV}/\text{\AA}$, respectively.

2.3. Catalytic performance

To perform the photocatalytic CO_2 reduction reactions, CoSn(OH)_6 ($3.6 \mu\text{mol}$) and $[\text{Ru}(\text{bpy})_3]\text{Cl}_2 \cdot 6\text{H}_2\text{O}$ ($10 \mu\text{mol}$, abbreviated as **Ru**) were added into a Schlenk flask reactor (80 ml in capacity) containing a mixture of TEOA/water/acetonitrile (1 ml/2 ml/3 ml). High purity CO_2 was introduced to the reactor with a partial pressure of 1 atm. The CO_2 reduction reactions were carried out at 30°C controlled by circulating water using a 300 W Xe lamp with a 420 nm cut-off filter as the light source under energetically stirring. After reaction for specific reaction time, the yields of products were determined by the Agilent 7820A gas chromatography.

3. Results and discussion

3.1. Material characterizations

The crystallographic structure and the phase purity of the CoSn(OH)_6 material were first studied by powder XRD. As shown in Fig. 1a, all the diffraction peaks of the synthesized CoSn(OH)_6 sample can be exactly indexed to a perovskite hydroxide phase (JCPDS card No.: 13-0356) [36], and the corresponding crystal structure of perovskite hydroxide CoSn(OH)_6 is illustrated in the insert in Fig. 1a. The sharp diffraction peaks reflect the high crystallinity of the sample. No other diffraction peaks are observed, indicating the phase purity of the CoSn(OH)_6 material. The chemical structures of the CoSn(OH)_6 sample are investigated by FTIR spectroscopy. In the FTIR spectrum (Fig. 1b), the broad band at 3208 cm^{-1} and the small pinnacle at 1638 cm^{-1} are designated to the stretching vibration and bending vibration of O–H bond, respectively [37,38]. The stretching vibration of Sn–O bond and the bending vibration of Sn–OH bond are correspondingly located at around 541 and 1177 cm^{-1} [37,38]. The strong band at 778 cm^{-1} signifies the H_2O – H_2O hydrogen bonding [37,38]. All the observation of XRD and FTIR measurements reveals that the crystal and chemical structures of perovskite hydroxide of CoSn(OH)_6 material are well developed [37,39,40].

FESEM and TEM were used to examine the morphology of the CoSn(OH)_6 material. The low magnification FESEM image shows that the as-

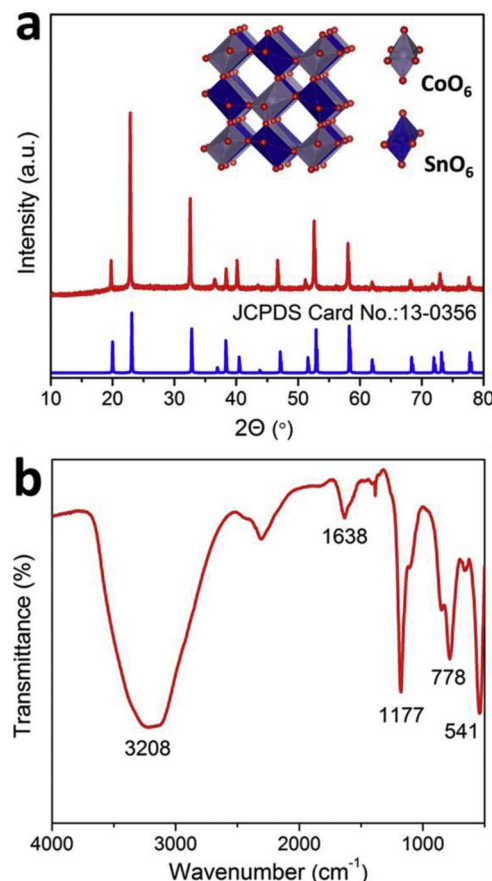


Fig. 1. (a) XRD pattern and (b) FTIR spectrum of CoSn(OH)₆ sample. Insert in (a) is the crystal structure of perovskite hydroxide CoSn(OH)₆.

synthesized CoSn(OH)₆ sample is consisted of uniform nanocubes without noticeable impurity particles or aggregates (Fig. 2a). The magnified FESEM image reveals that the average diameter of the nanocubes is *ca.* 200 nm with a smooth surface (Fig. 2b). TEM image presents the edge view of an individual CoSn(OH)₆ nanocube (Fig. 2c), and the high-resolution TEM (HRTEM) images display the visible lattice fringes (Inserts in Fig. 2c). The interplanar distance is determined to be *ca.* 0.385 and 0.444 nm, which corresponds to the (200) and (111) crystal planes of perovskite hydroxide CoSn(OH)₆, respectively. The selected area electron diffraction (SAED) pattern displays the regular array of diffraction spots (Fig. 2d), indicating the CoSn(OH)₆ nanocubes are single-crystalline [35]. The crystal structure of the as-prepared CoSn(OH)₆ sample revealed by TEM tests is in line with the results of XRD characterization. The chemical composition of the CoSn(OH)₆ sample is examined by EDX spectroscopic. As shown in Fig. 2e, only signal peaks of Co, Sn and O elements are detected, which further suggests the high purity of the CoSn(OH)₆ solid. Results of EDX elemental mappings confirm that all the composition elements are homogeneously distributed in the entire nanocube (Fig. 2f).

In order to study the surface chemical state of the elements in CoSn(OH)₆ sample, XPS characterizations are conducted. As revealed in Fig. 3a, the wide range XPS survey spectrum confirms the synthesized CoSn(OH)₆ material is composed of Co, Sn and O elements, which is in agreement with the results of EDX tests. Fig. 3b presents the Co 2p high-resolution XPS spectrum. The two peaks positioned at *ca.* 781.3 and 797.6 eV are assigned to Co 2p_{3/2} and Co 2p_{1/2}, respectively [37,41]. The characteristic shakeup satellite peak is located at *~*785.9 eV, which normally results from either the excitation of multielectron (shakeup) or the coupling between the unpaired electrons (multiplet splitting) [37,41]. Typically, the satellite peak of Co(III) is entirely absent, and the intensity of satellite peak in case of Co₃O₄ [*i.e.*, Co(II) and Co(III)] is very low. Thus, the strong intensity of the satellite peak indicates that the Co element holds the oxidation state of +2 in the CoSn(OH)₆ sample [37,39,41]. In the high resolution XPS spectrum of Sn 3d (Fig. 3c), the high intense peak with a binding energy of *ca.*

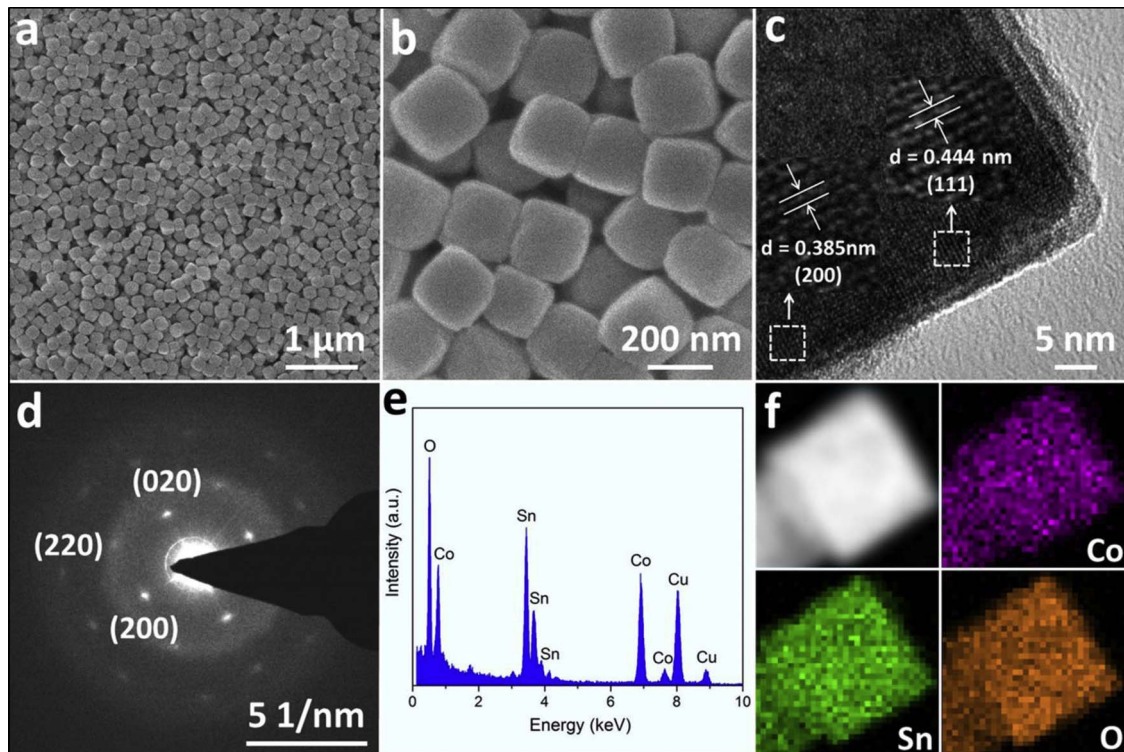


Fig. 2. (a, b) FESEM images, (c) TEM image, (d) SAED pattern, (e) EDX spectrum, and (f) TEM-EDX mappings of SnCo(OH)₆ nanocubes. Inserts in (c) are the corresponding HRTEM images.

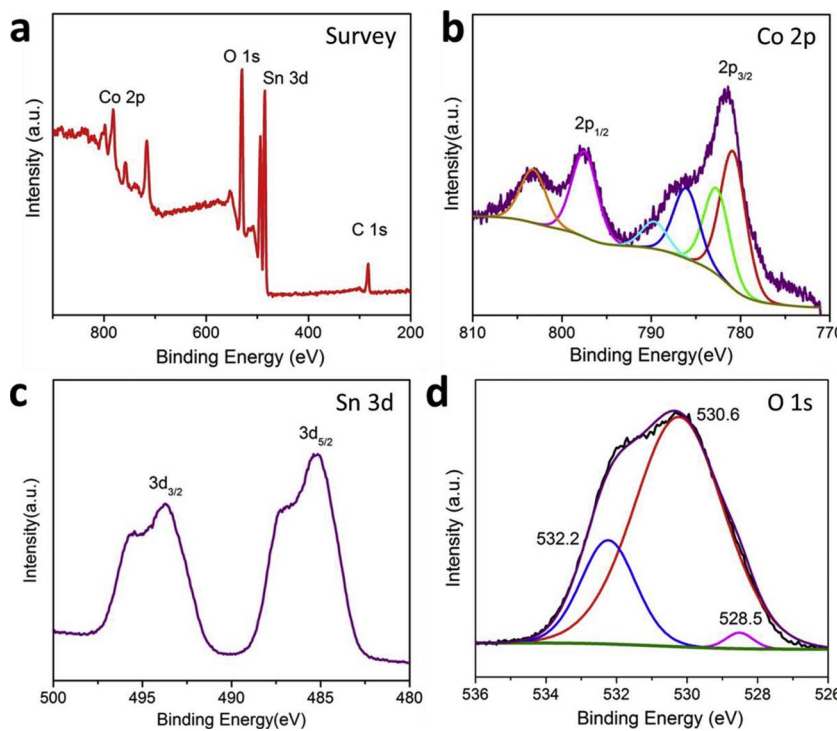


Fig. 3. XPS spectra of $\text{CoSn}(\text{OH})_6$ sample: (a) survey spectrum, (b) Co 2p, (c) Sn 3d, and (d) O 1s high resolution XPS spectra.

485.2 eV is Sn 3d_{5/2} and the peak located at 493.7 eV is Sn 3d_{3/2}. The peak splitting of Sn 3d is 8.5 eV, suggesting Sn is in a chemical state of Sn(IV) [37,41]. The O 1s high resolution XPS spectrum can be divided into three photoelectron peaks at 532.2, 530.6, and 528.5 eV (Fig. 3d), assigning to the oxygen of physically adsorbed water molecules, the lattice oxygen in perovskite hydroxide structure, and the oxygen of hydroxide ions, respectively [6,37,41].

The specific surface area and the pores size distribution of the $\text{CoSn}(\text{OH})_6$ nanocubes are investigated by N_2 sorption measurements. As shown in Fig. 4, the N_2 adsorption-desorption isotherms can be categorized as type IV with a type H1 hysteresis loop, pointing to the mesoporous characteristics. The BET specific surface area is calculated to be *ca.* 75 $\text{m}^2 \text{g}^{-1}$. The pore size distribution curve (Insert in Fig. 4) indicates that the $\text{CoSn}(\text{OH})_6$ nanocubes hold a pore size distribution of 2–16 nm with an average pore diameter of 3.5 nm. The presence of these mesopores is typically favorable to provide more catalytic-active sites, promote CO_2 adsorption and concentration, and facilitate mass/

charge transfers, and eventually enhance the performance of CO_2 reduction catalysis [6,28,42].

3.2. Theoretical calculations

To gain insights into the adsorption and activation behaviors of CO_2 molecules on the $\text{CoSn}(\text{OH})_6$ surface, periodic first-principles calculations based on density functional theory (DFT) are carried out. Fig. 5a shows the crystal structure of $\text{CoSn}(\text{OH})_6$, and the corresponding (100) surface is modeled by periodic slab consisting of five atomic layers. During the structural optimization, the atoms at the outermost three layers are fully relaxed in all directions, while other atoms at the remaining two layers are fixed to their bulk positions. The spacing between the adjacent slabs is set to about 15 Å.

After considering several arrangements of CO_2 molecule on the $\text{CoSn}(\text{OH})_6$ (100) surface, the most stable chemisorption structure is determined. As displayed in Fig. 5b, CO_2 molecule is adsorbed on the surface by two oxygen and carbon atoms, and three adsorption bonds, including C–O, Co–O and Sn–O bonds are found at the interface. The lengths of Co–O and Sn–O bonds are about 2.060, and 2.231 Å, respectively. After adsorption, with respect to the case in the gas phase, two C–O bonds of CO_2 are stretched about 0.10, and 0.12 Å, respectively, and meanwhile CO_2 moiety exhibits a bent configuration with the O–C–O angle of 127.1°. Since after adsorption the CO_2 exhibits a bent configuration like that of CO_2^- anion, the activation of carbon dioxide can be realized on the $\text{CoSn}(\text{OH})_6$ (100) surface.

3.3. Photocatalytic activity test

Catalytic performance of the $\text{CoSn}(\text{OH})_6$ nanocubes is evaluated by visible light driven CO_2 photoreduction reactions operated in H_2O -acetonitrile mixture under mild reaction conditions (30 °C, 1 atm CO_2) with Ru and triethanolamine (TEOA) as a photosensitizer and an electron donor, respectively. Fig. 6a shows the performance of CO_2 reduction catalysis under various reaction conditions. Under the typical conditions for 1 h reaction, the stable CO_2 molecules are photosplit into CO with a high generation of 18.7 μmol , coupled with a H_2 evolution of 3.0 μmol from the CO_2 reduction system. However, once without CoSn

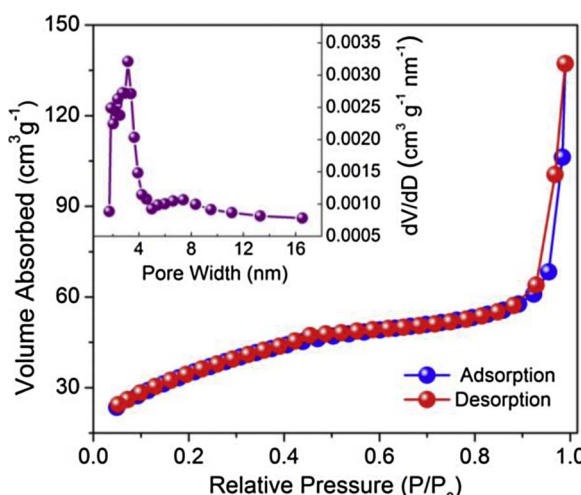


Fig. 4. N_2 adsorption-desorption isotherms of $\text{CoSn}(\text{OH})_6$ sample. Insert is the corresponding pore-size distribution curve.

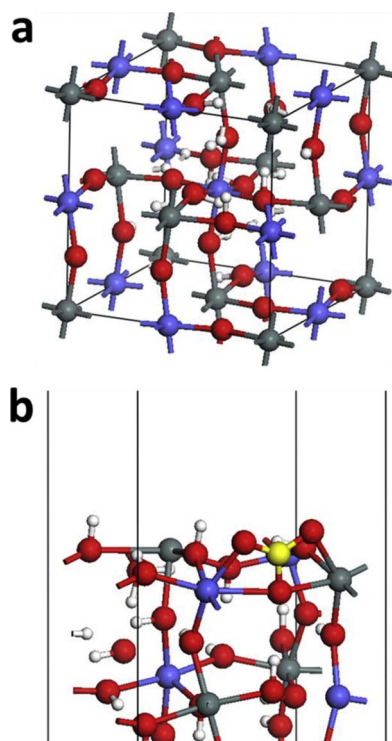


Fig. 5. (a) The structure of $\text{CoSn}(\text{OH})_6$ bulk and (b) the most stable configuration of CO_2 adsorbed on the (100) surface. The Co, Sn, O, C and H atoms are denoted by blue, dark gray, red, yellow and white spheres, respectively. (For interpretation of the references to color in this figure legend, the reader is referred to the web version of this article.)

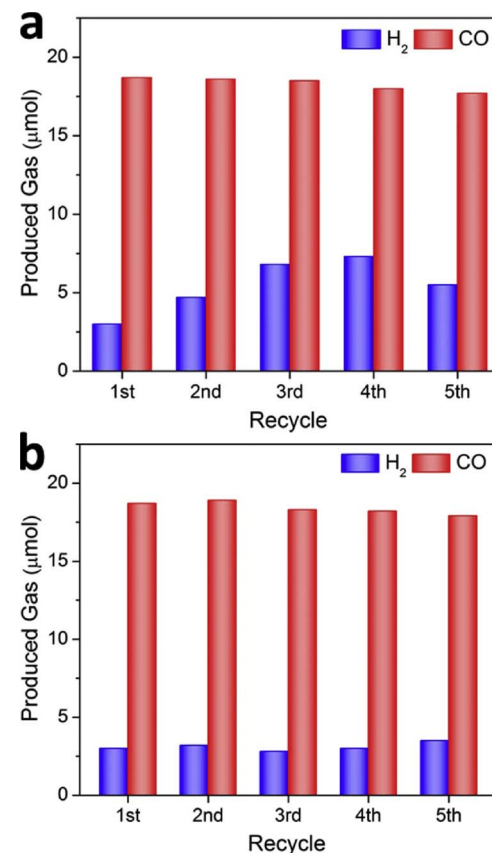


Fig. 7. Stability tests of $\text{CoSn}(\text{OH})_6$ catalyst. (a) Addition of the new dye into the system after 1 h reaction. (b) Recovery the used catalyst and then re-dispersion in a fresh reaction solution for consecutive reactions.

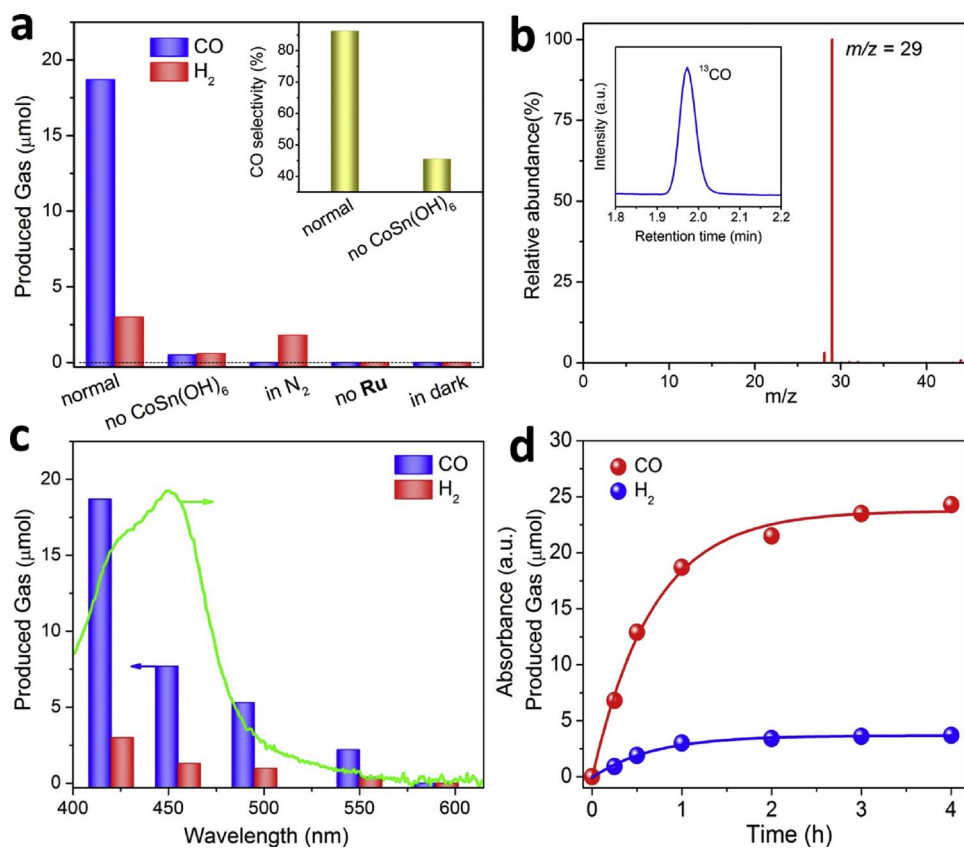


Fig. 6. (a) Yields of CO and H_2 from the CO_2 photoreduction system under various reaction conditions. Insert is CO selectivity under the corresponding conditions. (b) Results of GC-MS analysis for the produced CO from the $^{13}\text{CO}_2$ isotope experiment. (c) Wavelength dependence of production of CO and H_2 . (d) Time course of generation of CO and H_2 .

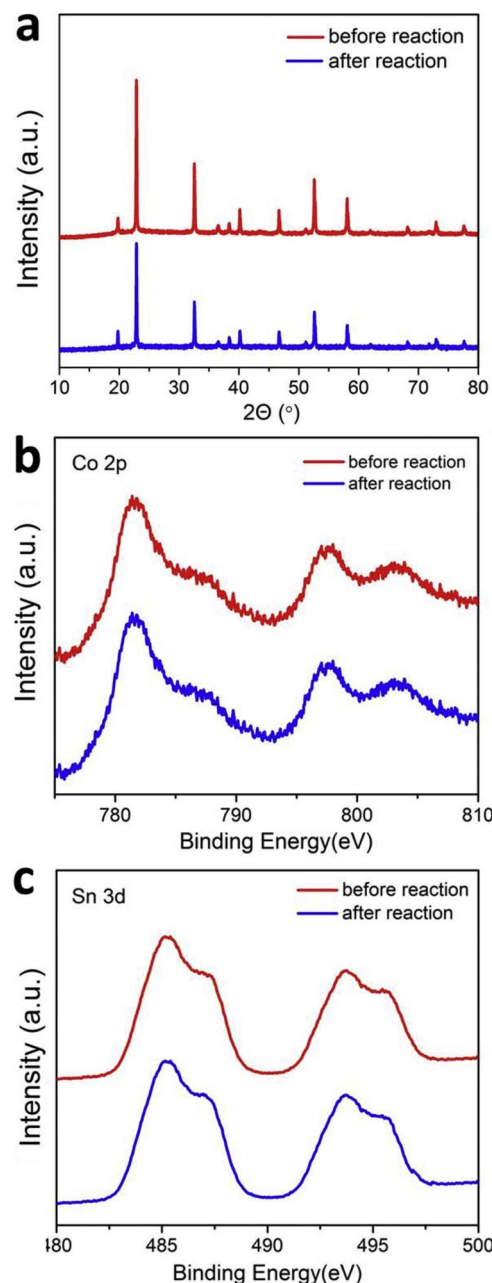


Fig. 8. (a) XRD patterns, (b) Co 2p and (c) Sn 3d high-resolution XPS spectra of used and fresh CoSn(OH)₆ samples.

(OH)₆ nanocubes as the catalyst for the system, the production of both CO (0.5 μmol) and H₂ (0.6 μmol) is substantially decreased. Besides, the selectivity of CO is also greatly reduced (Fig. 6a, Insert). These results strongly highlight the considerable catalytic efficiency of the perovskite hydroxide material for enhancing the CO₂-to-CO conversion reaction in the developed catalytic system. No other CO₂ reduction products (e.g., CH₄, CH₃OH, HCOOH) are detected from the reaction system, which is consistent with the results of reported works [11,12,21,27]. The control experiment using N₂ as the feedstock gas demonstrates that only a small amount of H₂ is generated, but without any formation of CO. This observation indicates that the CO product is originated from the CO₂ reactant. To further provide solid proof for the carbon source of CO, ¹³CO₂ isotope experiment is carried out. As shown in Fig. 6b, only ¹³CO with a *m/z* value of 29 is detected when using ¹³CO₂ as the feedstock gas, which firmly validates that the CO formation is generated from the splitting of CO₂ molecules. The production of CO and H₂ is greatly

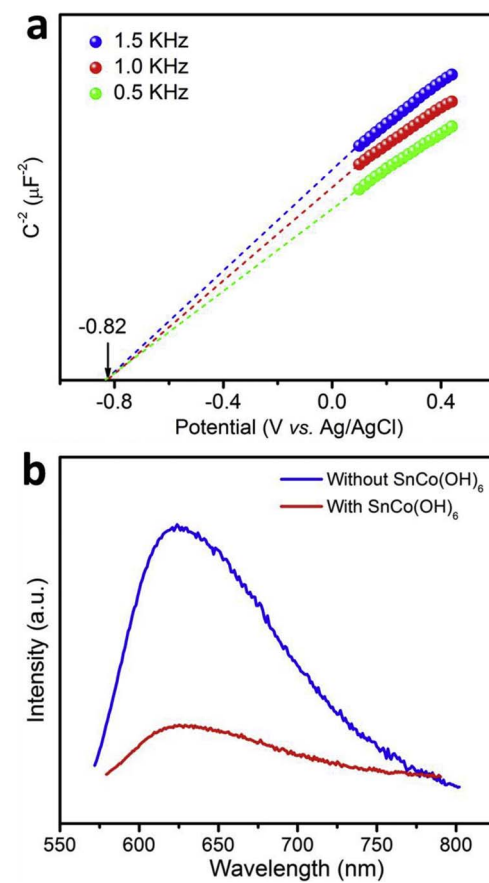
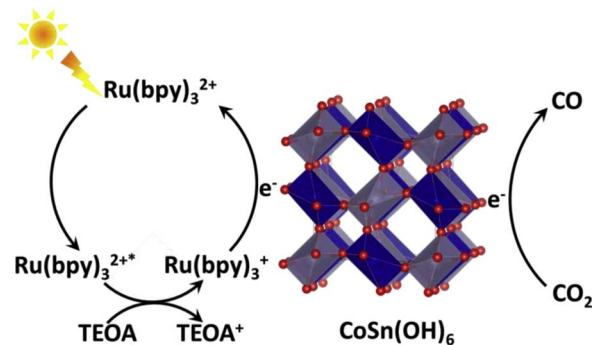


Fig. 9. (a) Mott-Schottky plots of CoSn(OH)₆ sample. (b) *In situ* PL spectra of the CO₂ photoreduction systems with and without CoSn(OH)₆ catalyst.



Scheme 1. Proposed possible reaction processes of perovskite hydroxide CoSn(OH)₆ catalyzed photocatalytic CO₂ reduction reaction.

influenced by the ratio of H₂O in the reaction solvent (Fig. S1, Supplementary materials), consistent with the results of reported works [6,7].

When the CO₂ reduction reactions are performed in absence of Ru photosensitizer or in dark (Fig. 6a), the reaction system is completely inactive to produce any product, which is a strong indication that the CO₂ conversion reaction proceeds by visible light irradiation. Furthermore, the performance of the catalytic system is also explored by light illumination of different wavelength. As displayed in Fig. 6c, it is found that the trend of CO/H₂ evolution matches well with the absorption spectrum of the ruthenium complex. This result confirms that CO₂ conversion reaction is operated photocatalytically by light absorption of the dye photosensitizer [6,9,12], producing excited charges for operating the subsequent redox reactions in the tandem catalytic CO₂ reduction system.

Studies on the reaction time demonstrate that the reaction system affords a high CO generation rate in the first 1 h reaction (Fig. 6d). Thereafter, the system gradually loses its high catalytic activity, due mainly to photobleaching of the Ru dye after limited catalytic runs, which is commonly observed in dye-sensitized photochemical reaction systems [28,30,43,44], but the $\text{CoSn}(\text{OH})_6$ catalyst is considered to be stable to preserve its intrinsic catalytic performance. To confirm this, after photoirradiation for 1 h, fresh photosensitizer is added into the system for consecutive reactions. As shown in Fig. 7a, the CO production reduced slightly and the yield of H_2 progressively improved in the first 4 runs. The reason for this observation is that the degradation of Ru photosensitizer generates ruthenium species to act as a H_2 -evolving catalyst [12]. In the fifth run, both yields of CO and H_2 diminish with addition of excessive amount of ruthenium complex, mainly because of the light-shielding effect [12].

Meanwhile, to further examine its stability, after photocatalysis the $\text{CoSn}(\text{OH})_6$ catalyst is filtrated, washed and reused for repeated reactions. As demonstrated in Fig. 7b, no obvious deactivation is found in five repeated operations. In the stability test, the total generation of the products is *ca.* 107 μmol , corresponding a catalytic turnover number (TON) of about 30 relative to $\text{CoSn}(\text{OH})_6$ catalyst for the CO_2 reduction system. This TON value is comparable to reported data [6,28,45,46].

In addition, after photocatalytic reactions, the used $\text{CoSn}(\text{OH})_6$ catalyst is removed and further characterized by XRD (Fig. 8a) and XPS (Fig. 8b, c). The results indicate that no noticeable change in crystal and surface structures is observed between the used and fresh $\text{CoSn}(\text{OH})_6$ samples. All these findings solidly highlight the high stability and reusability of the perovskite hydroxide $\text{CoSn}(\text{OH})_6$ material for CO_2 reduction catalysis in the photoredox system.

3.4. Discussion of mechanism

To explore the reaction mechanism of the CO_2 reduction reactions, the flat band potential of $\text{CoSn}(\text{OH})_6$ material is determined by Mott-Schottky analysis. As presented in Fig. 9a, the flat band potential of the $\text{CoSn}(\text{OH})_6$ catalyst is calculated to be *ca.* -0.62 V (vs. NHE), which is lower than the redox potential of $\text{E}(\text{Ru}(\text{bpy})_3^{2+*}/\text{Ru}(\text{bpy})_3^+) = -1.09$ V (vs. NHE) [47] and higher than that of $\text{E}(\text{CO}_2/\text{CO}) = -0.53$ V (vs. NHE) [48,49]. Therefore, the $\text{CoSn}(\text{OH})_6$ catalyst possesses the appropriate redox potential to accept the excited electrons from the reduced Ru complex to run the CO_2 -to-CO reduction reaction. Meanwhile, to demonstrate the efficient charge transfers of the CO_2 reduction system, *in situ* PL measurements are performed. As shown in Fig. 9b, the existence of $\text{CoSn}(\text{OH})_6$ catalyst can obviously inhibit the recombination of photoexcited charge carriers of the catalytic CO_2 conversion system, suggesting that the $\text{CoSn}(\text{OH})_6$ catalyst can indeed effectively accelerate charge migration for CO_2 reduction photocatalysis. In addition, the results of PL-decay analysis (Fig. S2, Supplementary materials) and transient photocurrent responses (Fig. S3, Supplementary materials) further support the function of $\text{CoSn}(\text{OH})_6$ catalyst for promoting charge transfer kinetics of the CO_2 photoreduction system. Based on the above results of photocatalytic evaluation and photo-/electro-chemical measurements, a possible reaction mechanism is thus proposed as follows (Scheme 1). Under visible light irradiation, the Ru photosensitizer is activated to the excited state, which is then reductively quenched by TEOA serving as sacrificial electron donor, forming the reduced photosensitizer. The reduced photosensitizer transfers electrons to the $\text{CoSn}(\text{OH})_6$ solid to operate subsequent reduction reactions. Finally, the CO_2 molecules absorbed on the surface of $\text{CoSn}(\text{OH})_6$ catalyst are reduced to CO. In the meantime, the excited electrons could also reduce the proton existed in the system to generate H_2 .

4. Conclusions

In summary, uniform perovskite hydroxide $\text{CoSn}(\text{OH})_6$ nanocubes

are synthesized by a facile one-pot co-precipitation method and systematically characterized by various physicochemical techniques. The $\text{CoSn}(\text{OH})_6$ solid is found by theoretical calculation to be capable of absorbing and activating CO_2 molecules on the (100) surface. For the first time, the $\text{CoSn}(\text{OH})_6$ nanocube material is developed as a cost-affordable, highly efficient and stable catalyst for enhancing the photosplitting of CO_2 into CO by the cooperation of a visible light photosensitizer. Under optimal reaction conditions, a high CO evolution rate of $18.7 \mu\text{mol h}^{-1}$ is achieved. The stability and reusability of the perovskite hydroxide catalyst for photocatalytic CO_2 conversion reactions are confirmed. Moreover, a possible reaction mechanism of the CO_2 reduction catalysis is also proposed based on the results of photocatalytic evaluation and photo-/electro-chemical measurements. This work may trigger considerable studies on perovskite-type materials and their semiconductor composites as active catalysts for photocatalytic CO_2 reduction toward artificial photosynthesis.

Acknowledgements

This work is financially supported by the National Key Technologies R & D Program of China (2014BAC13B03), the National Natural Science Foundation of China (21643009 and 21773030), the Open Project Program of the State Key Laboratory of Photocatalysis on Energy and Environment (Grant No. SKLPEE-KF201715), the State Key Laboratory of Photocatalysis on Energy and Environment (SKLPEE-2017B02), the Key Subject Building Project of Longyan University, and the IUI Cooperation Project of Longyan University (LC2016001).

Appendix A. Supplementary data

Supplementary data associated with this article can be found, in the online version, at <http://dx.doi.org/10.1016/j.apcatb.2017.11.035>.

References

- [1] C.K. Rofer-DePoorter, Chem. Rev. 81 (1981) 447–474.
- [2] W.J. Ong, L.L. Tan, Y.H. Ng, S.T. Yong, S.P. Chai, Chem. Rev. 116 (2016) 7159–7329.
- [3] N.S. Lewis, D.G. Nocera, Proc. Natl. Acad. Sci. U. S. A. 103 (2006) 15729–15735.
- [4] A. Listorti, J. Durrant, J. Barber, Nat. Mater. 8 (2009) 929–930.
- [5] T. Sakakura, J.C. Choi, H. Yasuda, Chem. Rev. 107 (2007) 2365–2387.
- [6] S. Wang, Y. Hou, X. Wang, ACS Appl. Mater. Interfaces 7 (2015) 4327–4335.
- [7] S. Wang, X. Wang, Appl. Catal. B: Environ. 162 (2015) 494–500.
- [8] W. Tu, Y. Zhou, Z. Zou, Adv. Mater. 26 (2014) 4607–4626.
- [9] R. Kuriki, M. Yamamoto, K. Higuchi, Y. Yamamoto, M. Akatsuka, D. Lu, S. Yagi, T. Yoshida, O. Ishitani, K. Maeda, Angew. Chem. Int. Ed. 56 (2017) 4867–4871.
- [10] S. Wang, J. Lin, X. Wang, Phys. Chem. Chem. Phys. 16 (2014) 14656–14660.
- [11] T. Ouyang, H.H. Huang, J.W. Wang, D.C. Zhong, T.B. Lu, Angew. Chem. Int. Ed. 56 (2017) 738–743.
- [12] S. Wang, W. Yao, J. Lin, Z. Ding, X. Wang, Angew. Chem. Int. Ed. 53 (2014) 1034–1038.
- [13] R. Kuriki, H. Matsunaga, T. Nakashima, K. Wada, A. Yamakata, O. Ishitani, K. Maeda, J. Am. Chem. Soc. 138 (2016) 5159–5170.
- [14] S. Wang, X. Wang, Angew. Chem. Int. Ed. 55 (2016) 2308–2320.
- [15] W.J. Ong, L.K. Putri, Y.C. Tan, L.L. Tan, N. Li, Y.H. Ng, X. Wen, S.P. Chai, Nano Res. 10 (2017) 1673–1696.
- [16] R. Kuriki, O. Ishitani, K. Maeda, ACS Appl. Mater. Interfaces 8 (2016) 6011–6018.
- [17] J. Qin, S. Wang, H. Ren, Y. Hou, X. Wang, Appl. Catal. B: Environ. 179 (2015) 1–8.
- [18] K. Maeda, R. Kuriki, M. Zhang, X. Wang, O. Ishitani, J. Mater. Chem. A 2 (2014) 15146–15151.
- [19] J. Lin, Y. Hou, Y. Zheng, X. Wang, Chem. Asian J. 9 (2014) 2468–2474.
- [20] C. Dong, M. Xing, J. Zhang, Mater. Horiz. 3 (2016) 608–612.
- [21] J.M. Lehn, R. Ziessel, Proc. Natl. Acad. Sci. U. S. A. 79 (1982) 701–704.
- [22] Z. Qin, C.M. Thomas, S. Lee, G.W. Coates, Angew. Chem. Int. Ed. 42 (2003) 5484–5487.
- [23] C.T. Cohen, T. Chu, G.W. Coates, J. Am. Chem. Soc. 127 (2005) 10869–10878.
- [24] H. Takeda, K. Ohashi, A. Sekine, O. Ishitani, J. Am. Chem. Soc. 138 (2016) 4354–4357.
- [25] J. Lin, Z. Pan, X. Wang, ACS Sustain. Chem. Eng. 2 (2014) 353–358.
- [26] V.S. Thoi, N. Kornienko, C.G. Margarit, P. Yang, C.J. Chang, J. Am. Chem. Soc. 135 (2013) 14413–14424.
- [27] C. Gao, Q. Meng, K. Zhao, H. Yin, D. Wang, J. Guo, S. Zhao, L. Chang, M. He, Q. Li, H. Zhao, X. Huang, Y. Guo, Z. Tang, Adv. Mater. 28 (2016) 6485–6490.
- [28] S. Wang, Z. Ding, X. Wang, Chem. Commun. 51 (2015) 1517–1519.
- [29] M. Jiang, Y. Gao, Z. Wang, Z. Ding, Appl. Catal. B: Environ. 198 (2016) 180–188.

[30] Z. Wang, M. Jiang, J. Qin, H. Zhou, Z. Ding, *Phys. Chem. Chem. Phys.* 17 (2015) 16040–16046.

[31] S. Wang, X. Wang, *Small* 11 (2015) 3097–3112.

[32] T. Takata, Y. Furumi, K. Shinohara, A. Tanaka, M. Hara, J.N. Kondo, K. Domen, *Chem. Mater.* 9 (1997) 1063–1064.

[33] N.J. Jeon, J.H. Noh, Y.C. Kim, W.S. Yang, S. Ryu, S.I. Seok, *Nat. Mater.* 13 (2014) 897–903.

[34] H. Kato, H. Kobayashi, A. Kudo, *J. Phys. Chem. B* 106 (2002) 12441–12447.

[35] Z. Wang, Z. Wang, H. Wu, X.W. Lou, *Sci. Rep.* 3 (2013) 01391.

[36] J.R. Neilson, J.A. Kurzman, R. Seshadri, D.E. Morse, *Inorg. Chem.* 50 (2011) 3003–3009.

[37] R. Sahoo, A.K. Sasmal, C. Ray, S. Dutta, A. Pal, T. Pal, *ACS Appl. Mater. Interfaces* 8 (2016) 17987–17998.

[38] S.L. Zhong, R. Xu, L. Wang, Y. Li, L.F. Zhang, *Mater. Res. Bull.* 46 (2011) 2385–2391.

[39] F. Song, K. Schenk, X. Hu, *Energy Environ. Sci.* 9 (2016) 473–477.

[40] H. Jena, K.G. Kutty, T. Kutty, *Mater. Chem. Phys.* 88 (2004) 167–179.

[41] J. Yang, H. Liu, W.N. Martens, R.L. Frost, *J. Phys. Chem. C* 114 (2009) 111–119.

[42] X. Wang, K. Maeda, X. Chen, K. Takanabe, K. Domen, Y. Hou, X. Fu, M. Antonietti, *J. Am. Chem. Soc.* 131 (2009) 1680–1681.

[43] R. Ziessel, J. Hawecker, J.M. Lehn, *Helv. Chim. Acta* 69 (1986) 1065–1084.

[44] J.M. Lehn, R. Ziessel, *J. Organomet. Chem.* 382 (1990) 157–173.

[45] Z. Chai, Q. Li, D. Xu, *RSC Adv.* 4 (2014) 44991–44995.

[46] G.A. Andrade, A.J. Pistner, G.P. Yap, D.A. Lutterman, J. Rosenthal, *ACS Catal.* 3 (2013) 1685–1692.

[47] C. Creutz, N. Sutin, *Inorg. Chem.* 15 (1976) 496–499.

[48] K. Kalyanasundaram, *Coord. Chem. Rev.* 46 (1982) 159–244.

[49] J. Schneider, H. Jia, J.T. Muckerman, E. Fujita, *Chem. Soc. Rev.* 41 (2012) 2036–2051.